Materials Today Bio 25 (2024) 100972

Contents lists available at ScienceDirect

Materials Today Bio

journal homepage: www.journals.elsevier.com/materials-today-bio

Dual-functional thermosensitive hydrogel for reducing infection and enhancing bone regeneration in infected bone defects

Yuhang Tian, Yutao Cui, Guangkai Ren, Yi Fan, Minghan Dou, Shaorong Li, Gan Wang, Yanbing Wang, Chuangang Peng, Dankai Wu *

Department of Orthopedics, The Second Hospital of Jilin University, Changchun, 130041, China

A R T I C L E I N F O

Keywords:
Antibacterial
Bone regeneration
Chitosan
Quaternized chitosan
Infected bone defect

A B S T R A C T

The contamination of bone defects is a serious therapeutic problem. The treatment of infected bone defects involves rigorous infection control followed by bone reconstruction. Considering these two processes, the development of biomaterials possessing antibacterial and osteogenic properties offers a promising approach for the treatment of infected bone defects. In this study, a dual-functional, thermosensitive, and injectable hydrogel composed of chitosan (CS), quaternized CS (QCS), and nano-hydroxyapatite (nHA) was designed, and the ratio of CS to QCS in the hydrogel was optimized to enhance the antibacterial efficacy of CS while reducing the cytotoxicity of QCS. *In vitro* studies demonstrated that the hydrogel with an 85 %:15 % ratio of CS to QCS exhibited excellent biocompatibility and antibacterial properties while also possessing suitable mechanical characteristics and degradability. The incorporation of nHA into the hydrogel enhanced MC3T3-E1 proliferation and osteogenic differentiation. Moreover, this hydrogel demonstrated superior *in vivo* therapeutic effectiveness in a rabbit model of infected bone defect. In summary, this study provides a promising material design and a comprehensive one-step treatment strategy for infected bone defects.

1. Introduction

Infected bone defects have always been an intractable problem in orthopedics clinics. The serious contamination at the defect site induces an inflammatory reaction, ultimately resulting in the formation of necrotic bone, which seriously hinders the process of bone regeneration and destroys the osteogenic microenvironment [1,2]. The current clinical treatment standard comprises controlling infection and bone regeneration [3,4]. The local bone defect could be further repaired once the infection is effectively managed. The clinical treatment of infection consists of debridement of the infected site followed by systemic application of antibiotics and implantation of antibiotic-impregnated bone cements such as polymethylmethacrylate (PMMA) beads [5]. However, some disadvantages such as insufficient local antibiotic concentration, antibiotic-resistant and extra surgery are inevitable [6]. For the bone reconstruction, although autogenous bone graft was considered as the gold standard in clinic treatment, it still faced the problems of insufficient donor source and many complications [7,8]. Allograft was also limited by immunologic rejection and reinfection [9]. Therefore, it is necessary to improve the treatment strategy of infected bone defects.

In the infected bone defect, implants and extracellular matrix provided the colonization site for bacteria. If bacteria colonized first, the process of bone regeneration would be severely hindered. Conversely, if osteoblasts first attached to the surface of the implants and subsequently mature and differentiate, the bacterial colonization can be inhibited and thus promoted bone repair [10,11]. Therefore, it is of great significance to construct a bioactive surface that can inhibit bacterial colonization and promote the adhesion, proliferation and differentiation of osteoblasts. As a cationic polymer, chitosan (CS) is one of the commonly used biomaterials, which possesses excellent biocompatibility, biodegradability and can exert antibacterial effect through direct contact with bacteria [12,13]. Moreover, the combination of CS and β-glycerophosphate (β-GP) enables the fabrication of temperature-responsive injectable hydrogel materials. It is known that CS is not a thermosensitive material, thermal gelation is accomplished by incorporating β-GP into the CS solution [14]. β-GP has been proven to be an osteogenic supplement of osteogenic medium and can inhibit the rapid precipitation of the hydrogel. The hydrophobic interaction between CS chain and glycerol group endows the CS with thermogelling characteristics at 37 °C [15,16]. CS/β-GP thermosensitive hydrogel can be implanted into

* Corresponding author.
E-mail address: wudk@jlu.edu.cn (D. Wu).

https://doi.org/10.1016/j.mtbio.2024.100972
Received 8 October 2023; Received in revised form 19 December 2023; Accepted 19 January 2024
Available online 20 January 2024

the defect site via minimally invasive injection locally, and its formation conditions are gentle while exhibiting a structure resembling that of the extracellular matrix, making it a suitable material for treating infected bone defects [17].

However, CS has poor water solubility and can only be protonated under acidic conditions, which greatly limits its function [18]. For this reason, the side chain of CS is usually modified to improve its properties [19,20]. Quaternized chitosan (QCS), a water-soluble CS derivative, was prepared by introducing quaternary ammonium groups into free hydroxyl or amino groups on CS [21]. Moreover, QCS exhibits excellent water solubility and enhanced antibacterial activity under physiological conditions, and has a good inhibitory effect on both *Escherichia coli* (*E. coli*) *and Staphylococcus aureus* (*S. aureus*) [22]. However, the single QCS has poor biocompatibility despite the augmented antibacterial property [23,24]. Therefore, the combination of CS and QCS can effectively offset their individual shortcomings. In addition, pure CS/QCS exhibits inadequate mechanical properties and stability, while also lacking the capacity to stimulate bone regeneration.

Nano-hydroxyapatite (nHA), a bioceramic containing calcium phosphate which has similar structure and chemical property to the minerals of the bone [25]. The excellent biocompatibility and osteoconductivity of nHA enable it to promote the osteointegration at the defect site and recruit osteoblasts [26]. However, its brittleness, low degradability and poor mechanical properties limited its application [27]. Thus, the hydrogel prepared by mixing CS and QCS with nHA could improve the mechanical properties, osteogenic properties and degradability.

In this study, we investigated an injectable thermosensitive hydrogel with dual functionalities encompassing antibacterial and osteogenic properties by incorporating β-GP into the mixed solution of CS and QCS, followed by the addition of nHA (Scheme 1). The excellent injectability of this hydrogel facilitates its minimally invasive injection into infected bone defects to avoid re-infection. And its thermosensitivity enables it to achieve gel state after injection without requiring additional intervention. Moreover, this biodegradable hydrogel exhibits simultaneous antibacterial and osteogenic properties upon implantation, providing a one-step approach for the treatment of infected bone defects and enhancing treatment efficacy. The morphology and mechanical properties of hydrogel would be studied. Moreover, the optimal proportions of CS and QCS that have good biocompatibility and effective antibacterial activity would be explored. In addition, *in vitro* experiments would be performed to investigate the antibacterial properties of the composite hydrogel and its ability to promote MC3T3-E1 proliferation and osteogenic differentiation. Subsequently, the composite hydrogel was implanted into infected radius defects in rabbits to evaluate its efficacy on bone repair *in vivo*.

2. Materials and methods

2.1. Materials

CS (medium molecular weight) and β-GP were purchased from Sigma-Aldrich (USA), QCS with degree of substitution 90 % and nHA were purchased from Aladdin Co., Ltd. (Shanghai, PR China), and phosphate-buffered saline (PBS) and 4 % paraformaldehyde were purchased from Solarbio (Beijing, PR China). High-glucose Dulbecco's Modified Eagle's Medium (HG-DMEM) and penicillin streptomycin double antibody were purchased from Gibco (Grand Island, NY, USA).

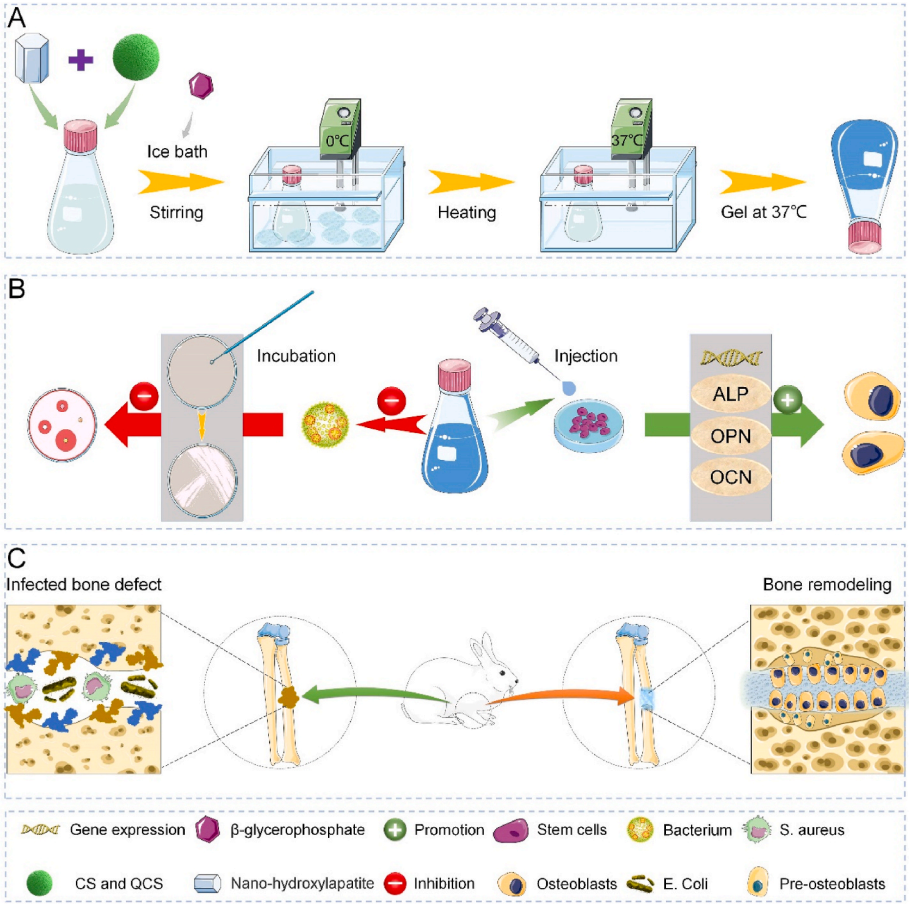

Scheme 1. Scheme illustration. A. Preparation of hydrogel. B. Culturing bacteria and cells with hydrogel *in vitro*. C. Injection of hydrogel into rabbit radial bone defect model and the process of antibacterial and osteogenesis.

Fetal bovine serum (FBS) was purchased from SenBeiJia Biological Technology Co., Ltd. (Nanjing, PR China). Trypsin-EDTA (0.05 % trypsin and 0.02 % EDTA) solution was purchased from Biosharp (Beijing, PR China). Cell Counting Kit-8 (CCK-8), calcein-AM-PI staining kit, RIPA lysis buffer, BCIP/NBT alkaline phosphatase (ALP) color development kit, and ALP assay kit were purchased from Beyotime Co., Ltd. (Shanghai, China). Osteogenic medium of mouse embryo osteoblast precursor cells (MC3T3-E1) and alizarin red stain were purchased from Cyagen (Santa Clara, USA). A FastPure Cell/Tissue Total RNA Isolation Kit, ABScript III RT Master Mix for qPCR with gDNA Remover, and Universal SYBR Green Fast qPCR Mix were obtained from Abclonal Co., Ltd. (Wuhan, PR China).

2.2. Preparation of the thermosensitive hydrogel

To prepare the pure CS/nHA thermosensitive hydrogel, CS powder (0.2 g) was dissolved in a 0.1 M solution of acetic acid (10 mL) at room temperature under continuous stirring until a clear solution formed. Subsequently, β-GP powder was dissolved in deionized water to prepare a β-GP solution (56 w/v%) and cooled at 4 °C for 30 min along with the CS solution. The β-GP solution was then carefully added dropwise to the CS solution under stirring in an ice bath for 15 min. The final volume ratio of CS to β-GP was 3:1. Next, nHA powder (50 mg) was introduced into the mixed solution under continuous stirring. The homogenized solution was incubated at 37 °C for 5 min in a constant-temperature water bath, resulting in the formation of a temperature-sensitive hydrogel. For the pure QCS/nHA hydrogel, the acetic acid in the above process was replaced with deionized water; the rest of the procedure was the same as above. To prepare hydrogels with different proportions of CS and QCS, CS and QCS were mixed in proportions of 85%–15 % and 90%–10 %, respectively, and then dissolved in 0.1 M acetic acid solution. The rest of the process was the same as above.

2.3. Characterization of the hydrogel

Scanning electron microscopy (SEM; Nova400, FEI, OR, USA) was used to study the porosity and surface morphology of the composite hydrogel. Fourier-transform infrared (FT-IR) spectra were acquired using a Spectrum One FT-IR spectrometer (Perkin Elmer) to analyze and compare the material of all hydrogel samples. The spectra were obtained at a resolution of 4.0 cm^{-1} with 32 scans per sample. The scanning range was 4000 to 400 cm^{-1}.

Rheological measurements of the hydrogel were performed to examine the elastic modulus and viscosity. A 200-μL sample of hydrogel was prepared and placed on a 25-mm parallel plate with a gap of 0.4 mm. The storage modulus and loss modulus of the hydrogel were then measured in the strain range of 0.1%–1000 % under stress detection mode. The temperature, angular velocity, and frequency were 25 °C, 6.28 rad/s, and 1 Hz, respectively. The shear viscosity and shear stress of the hydrogel were measured at 25 °C under shear rates ranging from 0.1 to 1000 s^{-1}. The dried hydrogel was immersed in a PBS solution at 37 °C, and the weight changes at different time points were recorded to assess the swelling ratio. In detail, the original dried hydrogel was recorded as W_0. After being immersed in PBS solution, the hydrogel was carefully extracted at a predetermined time point and subsequently weighed, recorded as W_t. The swelling ratio of the hydrogel was calculated as $[(W_t\text{-}W_0)/W_0] \times 100$ %.

Sprague Dawley (SD) rats were selected to examine the degradation and biocompatibility of the hydrogels. SD rats were anesthetized with isoflurane inhalation, and 0.5 mL of hydrogel was subcutaneously injected bilaterally into the dorsal region with an 18-G needle to form a gel depot. The rats were sacrificed at 0, 4, 7, 14, 21, 28, 35, and 42 days after injection to obtain back skin specimens for imaging and histological staining to assess the *in vivo* biocompatibility of the hydrogel. The gel state and weight were also recorded. Furthermore, the heart, liver, kidney and spleen were also collected after 42 days and fixed with tissue fixation solution to examine the impact of metabolism process of hydrogel on organs by H&E staining. Rats without any treatment were used as control group (CON).

2.4. In vitro cytocompatibility assay

Mouse embryo osteoblast precursor cells (MC3T3-E1) were grown in HG-DMEM containing 10 % FBS and 1 % penicillin and streptomycin. The cultured MC3T3-E1 cells were incubated at 37 °C in an atmosphere containing 5 % CO_2. Live/dead cell staining and CCK-8 assay were used to evaluate the biocompatibility of the hydrogel. The pure CS/nHA hydrogel (C/H), CS 85%-QCS 15 %/nHA hydrogel (C85-Q15/H), CS 90%-QCS 10 %/nHA hydrogel (C90-Q10/H), and pure QCS/nHA (Q/H) hydrogel were extracted in solution state (200 μL) and drawn into each well of untreated 24-well cell culture plates. After gelling at 37 °C, MC3T3-E1 cells were seeded at 1×10^4 cells/well in each group. The wells without hydrogel were considered as the control group (CON). Live/dead cell staining was conducted after co-culturing for 1 and 3 d. The working solution was prepared according to the manufacturer's instructions. The immersed samples were then cultured for 15 min at room temperature in the dark. Subsequently, the samples were washed twice with PBS to remove residual staining solution. The stained cells were observed using a fluorescent microscope.

For CCK-8 assay, MC3T3-E1 cells were co-cultured for 1, 3, and 7 d. The CCK-8 solution was added to each well at each time point, and each well was then incubated for 3 h at 37 °C with 5 % CO_2. The absorbance was then measured at 450 nm using a Bio-Rad microplate reader.

2.5. In vitro antibacterial activity

Antibacterial activity was evaluated using both quantitative and qualitative methods. *E. coli* (ATCC 25922) and *S. aureus* (ATCC 25923), representative Gram-negative and Gram-positive bacteria, were grown in Luria–Bertani broth in a shaking incubator (120 rpm) at 37 °C for one night until the optical density of the culture medium reached 0.5 at 600 nm, corresponding to approximately 4×10^8 colony forming units per mL (CFU/mL). Briefly, the bacterial suspension was diluted to 1×10^5 CFU/mL, and 200 μL of hydrogel was extracted from each group and co-cultured with bacteria. The bacterial suspension without any hydrogel was used as the negative control. After co-culturing for 4, 8, 12, 16, 24, 36, 48, 72, and 96 h, the optical density at 600 nm was detected, and the growth curve of bacteria was constructed. After culturing for 24 h in a 37 °C constant-temperature oscillation incubator, 100 μL of diluted bacterial solution was evenly spread on LB agar medium followed by incubation for another 16–18 h. The number of colonies was observed and quantitative analysis was employed to determine the antibacterial property by Image J software.

For live/dead staining assay of *E. coli* and *S. aureus*, 200 μL of hydrogel in each group was added into a 48-well culture plate followed by the addition of bacterial suspension (100 μL). After incubation for 24 h in an incubator, the antibacterial properties were qualitative analyzed according to the manufacturer's instructions. Fluorescence images were collected using confocal laser scanning microscopy. All experiments were conducted in triplicate to reduce the error rate.

2.6. Alkaline phosphatase (ALP) staining and activity analysis

To investigate the effect of each hydrogel on osteogenic differentiation, MC3T3-E1 cells were inoculated into six-well plates (CON, C/H, C85-Q15/H, and C90-Q10/H) at a density of 5×10^4 cells/well with osteogenic induction medium. After a 7-day incubation period, ALP staining and enzyme activity analysis were conducted. The cells were fixed with 4 % paraformaldehyde prior to ALP staining. The fixed samples were then washed two times with PBS and treated with BCIP/NBT staining working solution. After co-culturing for another 1 h in the dark at 25 °C, the samples were observed under microscope. To detect

the enzyme activity, RIPA lysis buffer was added to the well plate, and the supernatant was collected. The chromogenic substrate and diethanolamine buffer were then added to the sample and incubated at 37 °C for 30 min. Next, stop solution was added to each well, and a microplate reader was used to measure the absorbance at 405 nm. Finally, the ALP activity was determined by colorimetric analysis based on the absorbance.

2.7. Alizarin red staining

The MC3T3-E1 cells were seeded at a density of 5×10^4 cells/well in six-well plates in the CON, C/H, C85-Q15/H, and C90-Q10/H groups. After replacing the osteogenic induction medium, culturing was continued for14 d. At time point, the cells were rinsed twice with PBS and then fixed with 4 % paraformaldehyde for 30 min. Alizarin red solution was then added to each well and incubated for 30 min at room temperature. The samples were subsequently rinsed twice with PBS to remove residual staining solution, and the stained calcium nodules were observed. To quantify the amount of calcium nodules produced in the well plate, the stained calcium nodules were dissolved with 10 % cetylpyridinium chloride, and the absorbance at 540 nm was recorded.

2.8. RT-qPCR

To identify the expression levels of osteogenesis-related genes such as osteocalcin (*OCN*) and runt-related transcription factor (*RUNX2*), RT-qPCR was performed. For each group, MC3T3-E1 cells were seeded at 8×10^4 cells/well in 12-well plates with osteogenic induction medium for 7 d. Total RNA was obtained from each sample using the FastPure Cell/Tissue Total RNA Isolation Kit (Invitrogen, CA, USA), and cDNA was synthesized according to the manufacturer's instructions. Subsequently, qPCR amplification and detection were performed on a LightCycler 480 system using 2 × Fast SYBR Green Master Mix (Roche Diagnostics, Basel, Switzerland) with cDNA and primers. The primer sequences of the genes are shown in Table S1. The relative rates of mRNA expression were measured using the $2^{-\Delta\Delta Ct}$ approach and normalized to that of *GAPDH*.

2.9. In vivo animal experiments

2.9.1. Infected bone defect model in rabbits

All animal experimental procedures were approved by the Animal Care and Use Ethics Committee of Jilin University. The rabbit model of infected bone defect was established by surgically removing the middle segment of the right radius. Briefly, 30 five-month-old male New Zealand white rabbits with mature skeletons were randomly divided into three groups: CON, C/H, and C85-Q15/H ($n = 10$ in each group). Another three rabbits were selected for the sham operation group (untreated). After anesthetizing by the intramuscular injection of 50 mg/kg of 3 % (w/v) pentobarbital, a bone defect with a length of 1.5 cm was made in the middle of the radial shaft, and an absorbable gelatin sponge soaked in a solution containing *S. aureus* (1×10^7 CFU/mL) was then implanted into the defect site (CON group). For the C/H and C85-Q15/H groups, 0.2 mL of hydrogel was injected into the defect area after the implantation of the gelatin sponge. Following the completion of hydrogel implantation, the wound site was meticulously closed using absorbable sutures in a layered manner. To demonstrate the successful establishment of the infected bone defect model, the wound in the untreated group was sutured layer by layer without any additional interventions after exposing the radius. No post-operative antibiotics were given, and the bone infection in all groups persisted locally during the follow-up period. Samples of the radius were collected and preserved in 4 % polyformaldehyde solution at 8 and 12 weeks after surgery for further investigation.

2.9.2. Imaging examination

To evaluate the bone regeneration *in vivo* after hydrogel implantation, the radius was evaluated by X-ray at 8 and 12 weeks. The collected radial specimens were analyzed by micro-computed tomography (micro-CT; SkyScan 1076 scanner, Kontich, Belgium). After inserting the samples, the system was operated at 48 kV and 200 μA. The image pixel size for inspection was 18.26 μm. Using multimodal 3D visualization software, 3D reconstructions of the acquired images were obtained (NRecon 1.7.1.0 software, Kontich, Belgium). Image analysis was conducted using an analyzer for bones (CT Analyzer 1.17.7.2 software, Kontich, Belgium). The bone volume fraction (BV/TV), trabecular number (Tb. N), trabecular thickness (Tb. Th), and trabecular separation (Tb. Sp) in the designated region of interest (ROI) of the defect site were quantitatively analyzed.

2.9.3. Histological analysis

Radius samples were collected from each group and fixed in 4 % polyformaldehyde solution. After decalcification, the samples were embedded in paraffin and cut into sections. The samples were stained with hematoxylin and eosin (H&E), Giemsa stain, and Masson's trichrome stain. The stained sections were examined using a digital microscope (DSX 500; Olympus Corporation, Tokyo, Japan), and semi-quantitative analysis was carried out by estimating the surface area of new bone using Image J software.

2.9.4. Immunohistochemistry

The expressions of the osteogenesis-related proteins RUNX2 and OCN were detected in immunohistochemical experiments. The decalcified bone specimens were divided into tissue sections and then stained with anti-RUNX2 (ABclonal, catalog: A2851, Wuhan, China, 1:200) and anti-OCN (ABclonal, catalog: A14636, Wuhan, China, 1:200) antibodies. Hematoxylin was employed as a counterstain. The images of the specimens were obtained using a digital microscope, and Image J software was used to perform semi-quantitative analysis of the immunohistochemical staining images.

2.10. Statistical analysis

SPSS 19.0 (SPSS Inc., Chicago, USA) was used for statistical analysis. One-way analysis of variance was used to evaluate *in vitro* experimental results. The comparative *t*-test was used to examine *in vivo* experimental results. Differences with $p < 0.05$ were considered significant.

3. Results and discussion

3.1. Characterization of the hydrogel

Based on previous research, the ratio of CS to QCS in the blended hydrogel should exceed 83 %/17 % (w/w) for optimal performance, when the proportion of QCS in the mixture of CS and QCS exceeds 17 % (w/w), the hydrogel does not show thermosensitivity [28]. Therefore, to optimize the content of QCS for hydrogel performance, two ratios of CS/QCS (85 %/15 % and 90 %/10 %) were selected for further investigation in this study. After adding β-GP into the mixed solution, we successfully synthesized nHA hydrogels with different proportions of CS and QCS (Fig. 1A). The hydrogels exhibited good temperature sensitivity with a flowable liquid state occurring at 25 °C and a gel state at 37 °C. The addition of β-GP endowed CS with thermosensitivity, resulting in an increase in solution pH to the physiological range (7.0–7.4). Moreover, the immediate precipitation of the hydrated gel is effectively inhibited by β-GP [15]. As the SEM images show (Fig. 1B), the C85-Q15/H hydrogel had an obvious interconnected porous structure, and the pore size was in the range of 100–300 μm. The high-magnification images show nHA particles adhered to the pore wall. The microporous structure of the hydrogel closely resembles the pore size of human cancellous bone, which facilitates osteoblast adhesion and enables the efficient transport of cellular nutrients and waste [29–31].

FT-IR analysis was conducted on the C/H and C85-Q15/H hydrogels

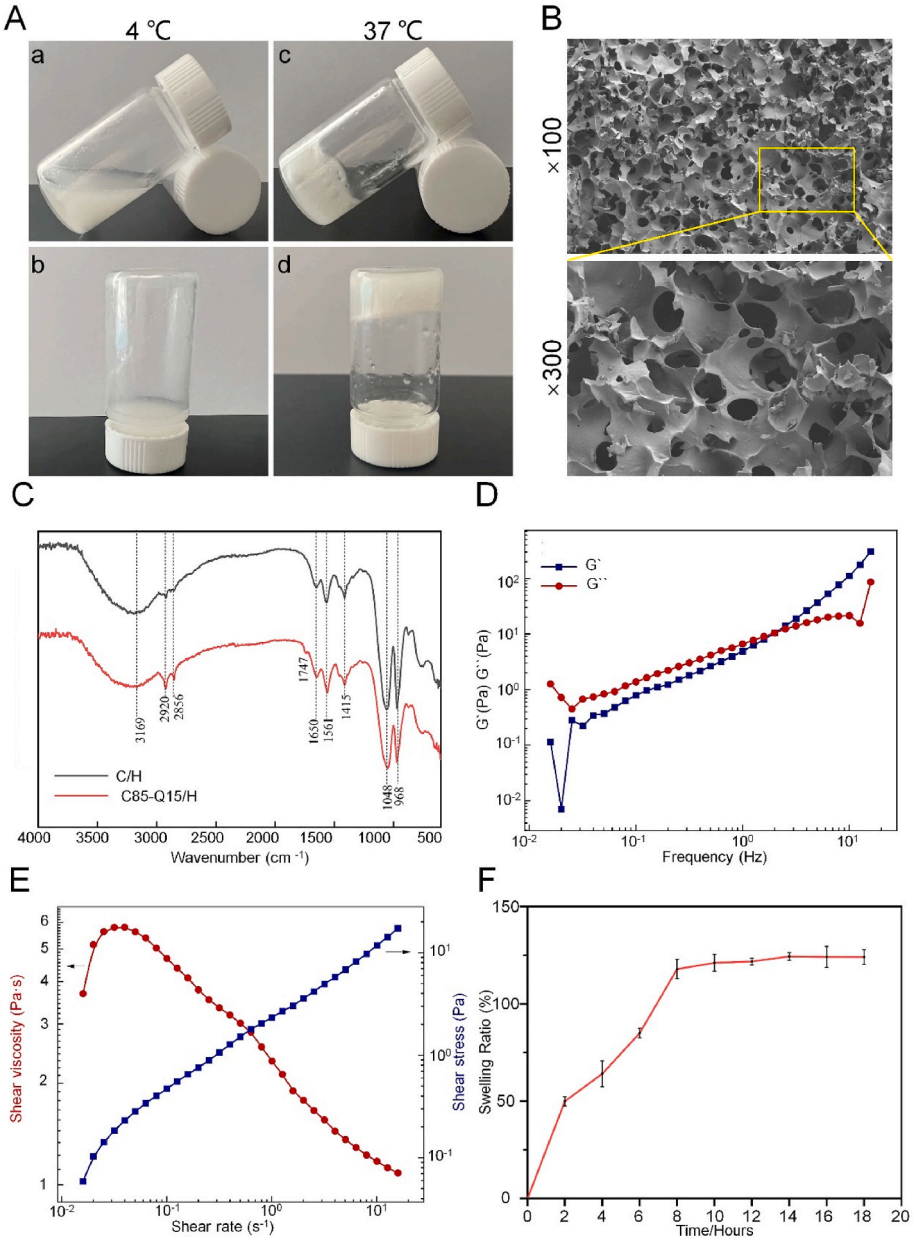

Fig. 1. Characterization of the hydrogels. A. Images of C85-Q15/H at 4 °C and 37 °C. B. Representative SEM images of C85-Q15/H. C. FT-IR spectra of C/H and C85-Q15/H. D, E. Storage and loss modulus properties of the C85-Q15/H hydrogel. F. Swelling kinetics of the C85-Q15/H hydrogel.

(Fig. 1C). The FT-IR spectrum of the C/H hydrogel (black) shows two characteristic peaks of CS and nHA. A prominent broad peak in the range of 3000–3500 cm^{-1} is primarily attributed to the stretching vibration of amino N–H and hydroxyl O–H groups within the CS structure, while the characteristic peak at 1415 cm^{-1} is associated with the C–H group in the CS main chain structure. The characteristic absorption peak of nHA corresponds to the stretching vibration of PO_4^{3-} and is observed at 1048 and 968 cm^{-1}. In the spectrum of C85-Q15/H (red), the slight shift of the broad peak from 3000 to 3500 cm^{-1} confirms the successful introduction of QCS because QCS contains more N–H groups than CS [32]. The positions of other peaks remain essentially identical to those of C/H, and the nHA characteristic peaks are also present, confirming the successful incorporation of various components in the hydrogel.

A hydrogel is a viscoelastic material that exhibits both energy storage and dissipation properties simultaneously [33]. As illustrated in Fig. 1D, with increasing strain strength, the storage modulus (G′) exceeds and remains higher than the loss modulus (G″), and the hydrogel can maintain its original gel state after deformation. Additionally, its storage modulus remains constant over time, demonstrating a high level of stability. As shown in Fig. 1E, the hydrogel exhibits shear thinning behavior, indicating excellent injectability and resistance to blockage during injection. The swelling kinetics of the C85-Q15/H was also evaluated under the condition of 37 °C. Fig. 1F showed that the good water absorption of C85-Q15/H reached the maximum of 118 % in about 8 h, and reached the swelling equilibrium in the later time. The ideal hydrogel should possess a specific water absorption capacity to mimic the tissue, facilitating nutrient transport, cell proliferation, and physiological functionality after the implantation of hydrogel [34]. Together with the results presented above demonstrated that the composite hydrogel possesses temperature responsiveness, a micro-porous structure conducive to cellular proliferation, and excellent injectability. These properties have substantial implications for the subsequent *in vitro* and *in vivo* validation experiments.

Moreover, the hydrogel showed good biodegradability and

biocompatibility *in vivo*. As shown in Fig. S1A, the C85-Q15/H hydrogel was almost completely degraded at 42 days after injection, confirming that the biodegradability was effectively promoted by combining nHA with CS and QCS. Moreover, the H&E staining of skin tissue showed that no inflammatory reaction occurred at the injection site, indicating the excellent *in vivo* biocompatibility of the hydrogel (Fig. S1B). It was reported that the degradation rate of CS/nHA scaffolds slowed down after nHA was added, which was related to the interaction between CS and nHA molecules [35,36]. The CS and QCS possessed cationic and amino hydroxyl functional groups, enabling them to interact with the anionic surface of nHA, this interaction enhanced the stability of hydrogel. In addition, the nHA molecule had high crystallinity and stability, which changed the chemical composition and structure of hydrogel so that the degradation can be sustained [37]. The slow degradation of materials was beneficial to infection control and bone regeneration. Furthermore, the degradation products of CS, QCS and HA composites were mainly non-toxic substances, such as glucose, amino sugar and phosphate, which can be metabolized and excreted by human body [38]. The hydrogel did not produce immune rejection, which is of great significance for bone healing at defect sites. We also studied whether the C85-Q15/H had toxic effect on main organs of SD rats. The H&E staining showed that the organs in the C85-Q15/H exhibited no inflammatory reaction and hemolysis compared to the CON group (Fig. S2). These results further indicated that C85-Q15/H was safe as a biomaterial for treating infected bone defects *in vivo*.

3.2. Biocompatibility of the composite hydrogels

To investigate the effect of QCS content on biocompatibility, we assessed the effects of the C/H, C85-Q15/H, C90-Q10/H, and Q/H hydrogels on MC3T3-E1 cell viability and proliferation by conducting Live/dead cell staining and CCK-8 experiments. The wells without hydrogel were considered as the control group. As shown in Fig. 2A, the number of living cells in all groups except for the Q/H group was significantly higher on day 3 compared to on day 1. Conversely, the number of dead cells increased remarkably from day 1 to day 3 in the Q/H group. These findings suggest that hydrogels composed of pure QCS possess potent cytotoxicity and are unsuitable for bone tissue engineering. Similarly, in CCK-8 assays to quantitatively analyze the effects of hydrogels on cell proliferation, excellent growth was observed within 7 days in all groups except the Q/H group (Fig. 2B). The Q/H hydrogel exhibited an inhibitory effect on MC3T3-E1 cell proliferation, leading to a gradual decrease in the number of cells from days 1–7. Meanwhile, no statistically significant differences in cell numbers were observed among the C/H, C85-Q15/H, and C90-Q10/H groups, suggesting that these hydrogels had minimal adverse effects on cell proliferation and supported favorable growth. The experimental results are consistent with those of previous studies, that is, the pure Q/H hydrogel with a high content of QCS is highly toxic to cells, which may be related to the mitochondrial damage of cells [24,39]. The above results further support the notion that adjusting the proportions of CS and QCS can effectively mitigate the cytotoxicity induced by QCS, thereby enhancing the biocompatibility of the system. The gel-forming performance remained unaffected by the mixing ratio.

3.3. In vitro antibacterial activity assay

The optical density (OD_{600}) values of the bacterial liquid were measured at various time intervals while co-culturing *E. coli* and *S. aureus* with the C/H, C85-Q15/H, C90-Q10/H, and Q/H hydrogels. As shown in Fig. 3A and B, the OD_{600} values of *E. coli* and *S. aureus* increased over time in the CON and C/H groups. Although initially effective at inhibiting bacterial proliferation, the C/H hydrogel eventually lost its antibacterial efficacy, and the bacteria grew slowly. In

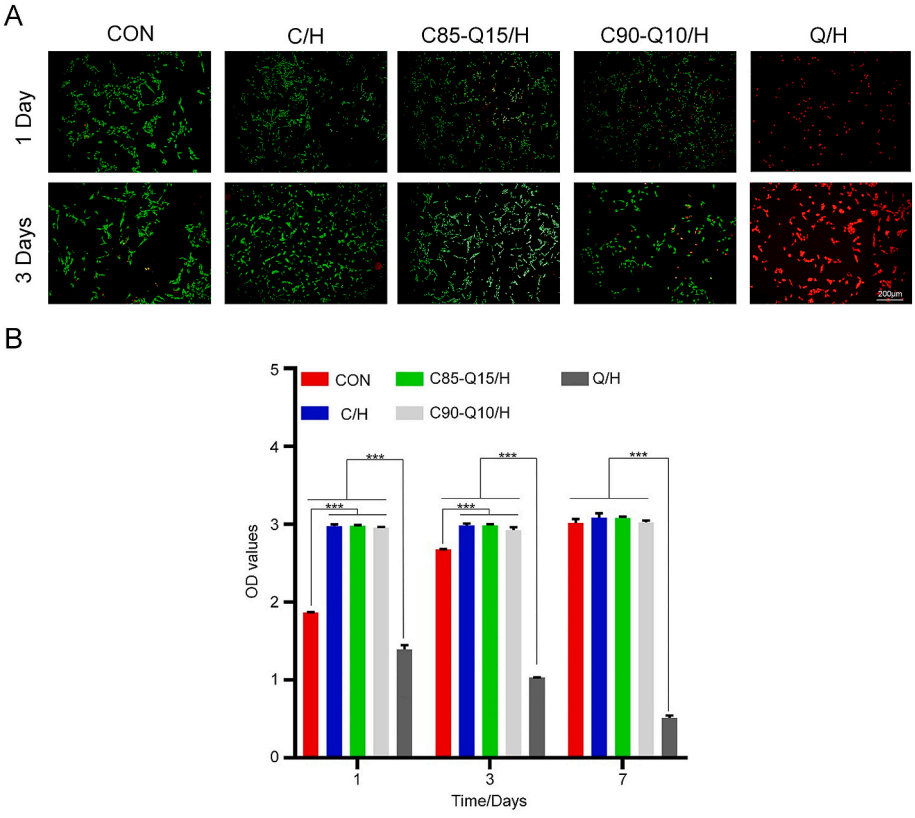

Fig. 2. Viability of MC3T3-E1 cells incubated with different hydrogels. A. Live/dead cell staining images. B. CCK-8 assay results for MC3T3-E1 cells in each group of hydrogels (***, $p < 0.001$) (Data are expressed as mean ± SD ($n = 3$)).

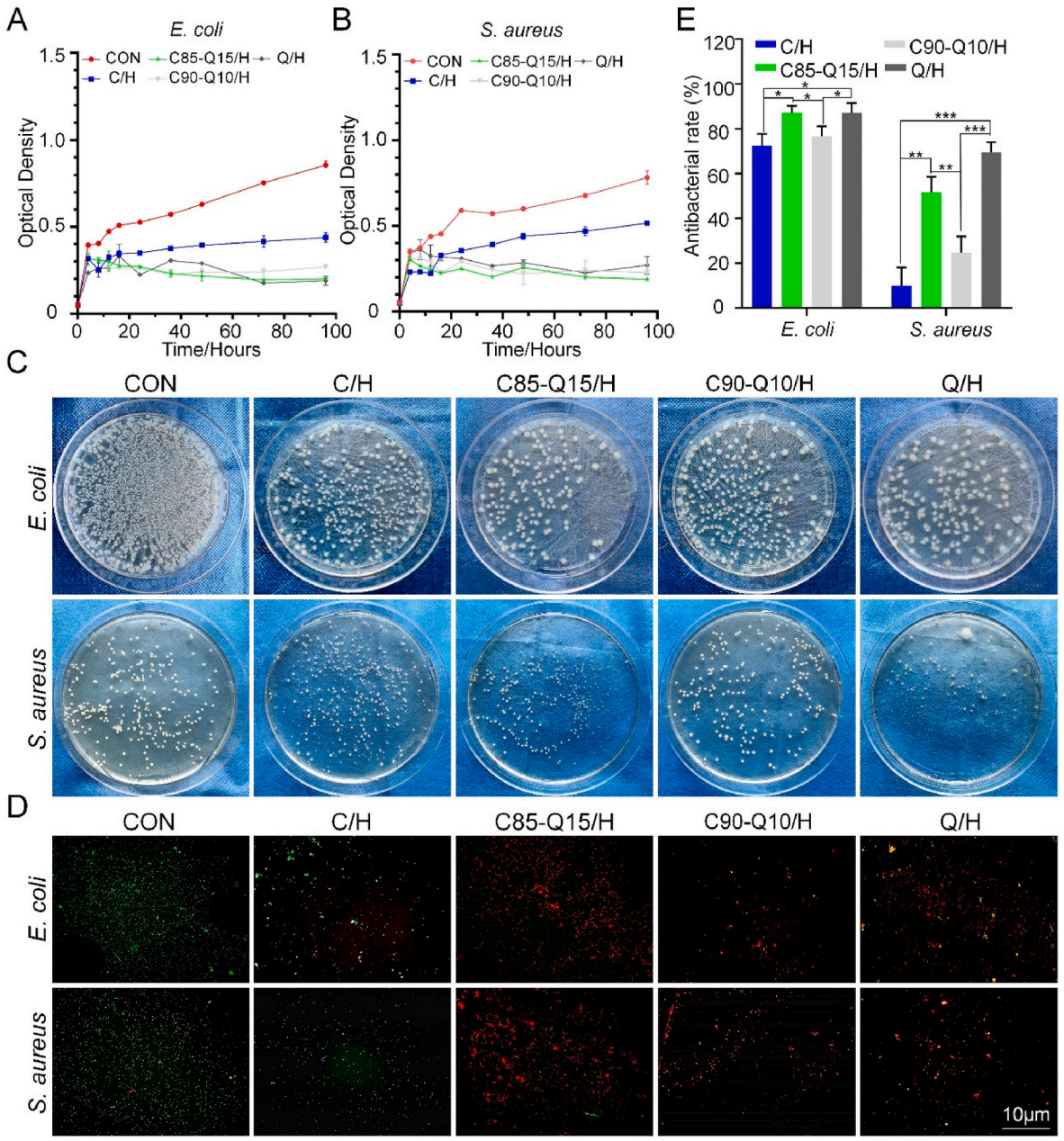

Fig. 3. Antibacterial activities of C/H, C85-Q15/H, C90-Q10/H, and Q/H against *E. coli* (A) and *S. aureus* (B) after co-culturing for 96 h. C. Agar plate experiment after 24 h of co-culturing with *E. coli* and *S. aureus*. D. Live/dead bacterial staining images at 24 h. E. Quantitative analysis of agar plate cultures experiment (*, $p < 0.05$; **, $p < 0.01$; ***, $p < 0.001$) (Data are expressed as mean ± SD ($n = 3$)).

contrast, the OD_{600} values in the C85-Q15/H, C90-Q10/H, and Q/H groups decreased over time for both bacteria. For *E. coli*, the OD_{600} values in the C85-Q15/H, C90-Q10/H, and Q/H groups at 96 h were 0.20 ± 0.01, 0.26 ± 0.01, and 0.19 ± 0.02, respectively, significantly higher than those in the C/H (0.44 ± 0.02) and CON (0.86 ± 0.02) groups ($p < 0.001$). While there was little difference in OD_{600} values between C85-Q15/H and C90-Q10/H ($p > 0.05$), both of which were higher than C90-Q10/H ($p < 0.01$). The C85-Q15/H, C90-Q10/H, and Q/H hydrogels exhibited durable antibacterial activity against *S. aureus* and maintained their antibacterial efficacy for up to 96 h. At 96 h, the OD_{600} values in the C85-Q15/H, C90-Q10/H, and Q/H groups were 0.19 ± 0.01, 0.23 ± 0.04, and 0.27 ± 0.04, respectively. The OD_{600} values of the C85-Q15/H, C90-Q10/H, and Q/H groups were not significantly different ($p > 0.05$), and they were significantly higher than those of the CON (0.78 ± 0.03) and C/H (0.52 ± 0.01) groups ($p < 0.001$).

To further investigate the specific inhibition of the hydrogels for the two bacterial strains, agar plate cultures were conducted at designated time points (Fig. 3C). Compared to the CON group, the number of *E. coli* colonies after co-culturing for 24 h was significantly lower in the hydrogel groups and particularly in the C85-Q15/H and Q/H groups. Additionally, the reduction in the number of *E. coli* colonies was greater in the Q85-Q15/H and Q/H groups compared to the C/H and C90-Q10/H groups. Notably, the numbers of colonies of *S. aureus* in the C85-Q15/H and Q/H groups w lower than in the C90-Q10/H and C/H groups. The antibacterial rate of each hydrogel was then examined. As shown in Fig. 3E, the antibacterial rate of C85-Q15/H and Q/H against *E. coli* achieved 87.17 ± 2.48 % and 87.20 ± 3.51 %, respectively, which was higher than that of C/H (54.41 ± 4.29 %) and C90-Q10/H (57.43 ± 3.75 %) groups ($p < 0.05$). However, there was no statistically difference between C85-Q15/H and Q/H. As for *S. aureus*, the antibacterial rate of

Q/H was 69.47 ± 3.75 %, which was significantly higher than that of C/H (10.02 ± 6.59 %) and C90-Q10/H (24.60 ± 5.99 %) groups ($p < 0.001$). Moreover, the antibacterial rate of C85-Q15/H achieved 51.80 ± 5.53 %, which was also higher than that of C/H and C90-Q10/H ($p < 0.01$). These results indicated that the augment of QCS concentration can increase the inhibitory effect on *E. coli* and *S. aureus*.

Intuitive evidence of antibacterial activity can also be observed in the live/dead bacterial staining images (Fig. 3D). In all three groups of hydrogels containing QCS, significant red fluorescence (indicating dead bacteria) was detected, and only a few spots of green fluorescence (indicating live bacteria) were observed. Especially in the C85-Q15/H and Q/H groups, a high level of red fluorescence indicating dead *E. coli* and *S. aureus* was clearly observed. The C/H group showed comparatively higher levels of green fluorescence for both *E. coli and S. aureus* than the other three groups. This further supports the limited antibacterial ability of the pure CS hydrogel.

CS and QCS have been extensively studied as antibacterial materials, and QCS exhibits stronger antibacterial properties than CS due to its highly cationic nature [40,41]. Our findings clearly validate that when used as an antibacterial material alone, the C/H hydrogel has insufficient antibacterial duration and strength against *E. coli* and *S. aureus*. In contrast, after mixing CS with QCS in different proportions, the hydrogels exhibited strong antibacterial properties. This may be related to the high density of positive charges in the QCS structure. These positive charges allow QCS to be adsorbed on the surfaces of negatively charged bacteria, leading to the leakage of proteins and other cell components in a dose-dependent manner [4,42,43]. Moreover, QCS had greater efficacy against gram-positive bacteria than gram-negative bacteria. This is because the cell wall of *S. aureus* is solely formed of peptide polygen, whereas the cell wall of *E. coli* is composed of peptide polygen plus an outer lipopolysaccharide layer that acts as a barrier targeting large-molecular-weight molecules [44]. Although the Q/H hydrogel showed a significant antibacterial effect against both *E. coli* and *S. aureus*, its cytotoxicity makes it unsuitable for the treatment of infected bone defects. Thus, in the subsequent *in vitro* osteogenesis experiments, we excluded the Q/H hydrogel and evaluated the osteogenic differentiation performances of the C85-Q15/H, C90-Q10/H, and C/H hydrogels.

3.4. Osteogenic effects of hydrogels in MC3T3-E1 cells

To investigate the effects of the composite hydrogels on the osteogenic differentiation of MC3T3-E1 cells, we conducted ALP staining assay and activity analysis after 7 d of osteogenesis induction. As shown in Fig. 4A(a), compared with the C90-Q10/H, C/H, and CON groups, a higher number of positively stained cells and a darker staining color were observed in the C85-Q15/H group. In the C90-Q10/H group, more ALP-positive cells were observed than in the C/H and CON groups. Compared with the CON group, the number of ALP-positive cells was higher in the C/H group. The ALP activity in the C85-Q15/H group (2.33

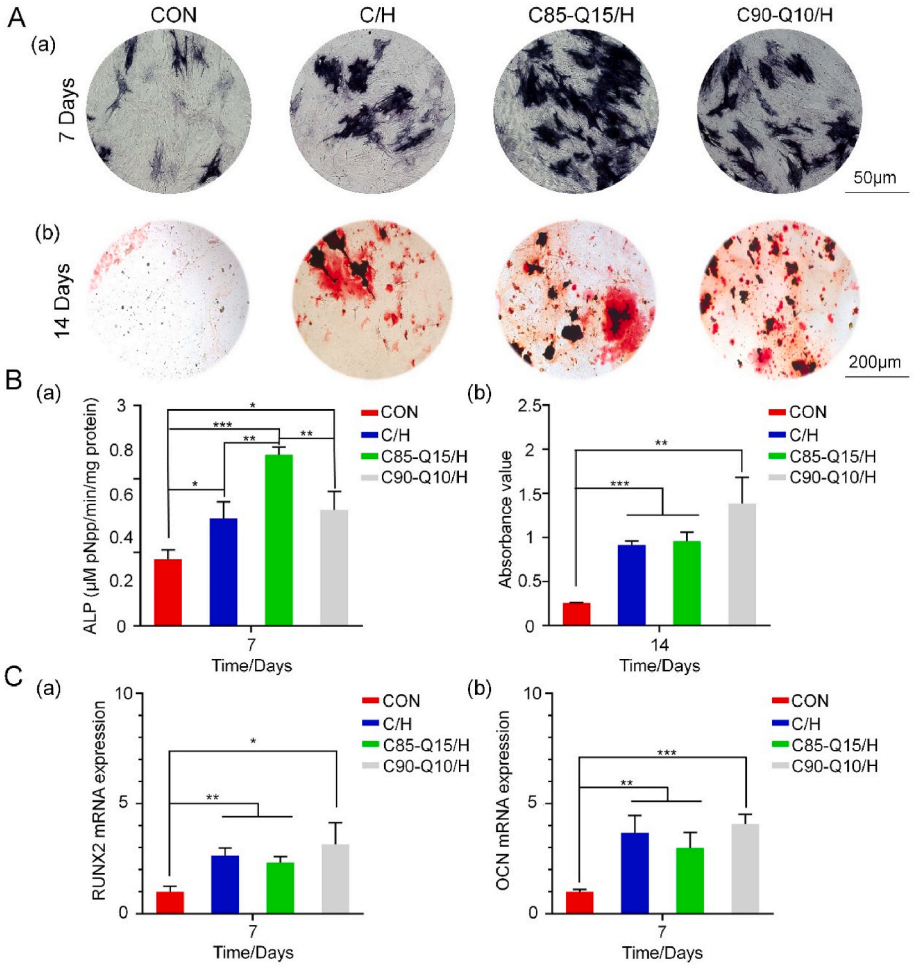

Fig. 4. Osteogenic properties of the C/H, C85-Q15/H, and C90-Q10/H hydrogels. A. (a) ALP staining images at 7 d after induction. (b) Alizarin red staining at 14 d after induction. B. (a) Quantitative analysis of ALP enzyme activity. (b) Semi-quantitative analysis of calcium nodules based on the absorbance at 450 nm. C. (a) RT-qPCR results for *RUNX2* at 7 d after induction. (b) RT-qPCR results of *OCN* at 7 d after induction (*, $p < 0.05$; **, $p < 0.01$; ***, $p < 0.001$) (Data are expressed as mean ± SD ($n = 3$)).

± 0.09 μM pNpp/min/mg protein) was higher than those in the C/H and C90-Q10/H groups (1.46 ± 0.18 and 1.58 ± 0.20, respectively; $p < 0.01$). Moreover, compared to the CON group (0.91 ± 0.10 μM pNpp/min/mg protein), the ALP activity was higher in both the C90-Q10/H and C/H groups [$p < 0.05$; Fig. 4B(a)].

Subsequently, we conducted alizarin red staining and semi-quantitative analysis to assess the effects of the composite hydrogels on the deposition of calcium in MC3T3-E1 cells. As is shown in Fig. 4A (b), red calcium nodules were more prominently observed in the C/H, C85-Q15/H, and C90-Q10/H groups compared to the CON group on day 14. Notably, among the groups, the calcium nodules in the C85-Q15/H and C90-Q10/H groups exhibited the deepest staining color and largest stained area. The semi-quantitative analysis of the calcium nodules confirmed the above results; the absorbance values in the C85-Q15/H and C90-Q10/H groups on day 14 were 0.96 ± 0.08 and 1.39 ± 0.24, respectively ($p > 0.05$), both of which were higher than the absorbance in the CON group [0.27 ± 0.03; $p < 0.001$ and $p < 0.01$, respectively; Fig. 4B(b)]. The absorbance value in the C/H group was 0.91 ± 0.04, which was not significantly different from those in the C85-Q15/H and C90-Q10/H groups ($p > 0.05$) and higher than that of the CON group ($p < 0.001$).

ALP is a primary indicator of early mineralization in the extracellular matrix. ALP facilitates the hydrolysis of organophosphorus compounds and regulates the metabolism of Ca^{2+} and PO_4^{3-} to promote bone mineralization [30,45]. The results of ALP staining assay and activity analysis confirmed that all three hydrogels promoted the osteogenic differentiation of MC3T3-E1 cells to some extent, with the C85-Q15/H group demonstrating the most pronounced effect in early differentiation. This may be related to the 15 % QCS content, which facilitates cell spreading and proliferation on the hydrogel and is beneficial to enhancing ALP activity [46]. In addition, the introduction of nHA improved osteogenic differentiation, and quaternization can weaken intermolecular hydrogen bonds, promote interactions between QCS and nHA ions, and attract PO_4^{3-}, thus improving the early osteogenic ability [47,48]. Calcium nodules are the mineralized matrix secreted by osteoblasts; an increase in nodules represents the deposition of minerals and is an important sign of osteoblast maturation in the later stage of osteogenesis [49,50]. The concentration of nHA in the three hydrogels was consistent, and the hydrogel materials were clearly washed by DDH_2O before staining to avoid interference [51]. Therefore, we can confirm that QCS mainly promoted osteogenesis in the early stage by accelerating the deposition of Ca^{2+} through its positive charge. However, after the rapid deposition of apatite, nHA particles endow the hydrogel with excellent osteogenic and mineralization ability [52].

We also analyzed osteogenesis-related genes such as *RUNX2* and *OCN* by conducting RT-qPCR experiments. *RUNX2* is an early indicator of osteogenic differentiation and belongs to the *RUNX* family, which plays a crucial role in both osteogenic differentiation and maintaining bone maturation of mesenchymal stem cells [53]. As the primary regulator of osteogenesis, *RUNX2* is essential for regulating the downstream expressions of genes such as *OCN* [54]. *OCN* is capable of regulating bone calcium metabolism, and its up-regulation can enhance the formation of mineralized calcium nodules [49]. As illustrated in Fig. 4C (a), the expressions of *RUNX2* in the C/H and C85-Q15/H groups were 2.64 ± 0.28 and 2.32 ± 0.23 fold higher than that of the CON group, respectively ($p < 0.01$). The expression of *RUNX2* in the C90-Q10/H group was 3.14 ± 0.81 fold higher than that in the CON group. No significant differences in the expressions of *RUNX2* were observed among the three hydrogels. The expression of *OCN* was similar to that of *RUNX2* on day 7, and the *OCN* expression in the C90-Q10/H group was 4.08 ± 0.36 fold higher than that in the CON group ($p < 0.001$). The *OCN* expressions in the C/H and C85-Q15/H groups were 3.68 ± 0.64 and 2.99 ± 0.58 fold higher than that in the CON group, respectively ($p < 0.01$). However, no significant differences in the expressions of *OCN* were observed among the three hydrogel groups [$p > 0.05$; Fig. 4C(b)].

After the addition of nHA, the composite hydrogels realized higher osteogenic capability. On the other hand, the strong cationic nature of QCS can bind to negatively charged proteins and lipids on the osteoblast surface to promote adhesion, which facilitates early osteogenic differentiation [24,30]. In summary, the *in vitro* experiments confirmed that the hydrogel obtained by mixing CS and QCS in different proportions had better antibacterial properties than the pure CS hydrogel. Specifically, the C85-Q15/H hydrogel displayed the highest antibacterial efficacy against both *E. coli* and *S. aureus* while maintaining non-cytotoxicity. Moreover, the C85-Q15/H hydrogel could promote early osteogenesis and up-regulate osteogenesis-related genes. These properties meet the standard for biological scaffolds. Therefore, we selected the C85-Q15/H and C/H hydrogels as the experimental and control materials, respectively, to further confirm the efficacy of the C85-Q15/H hydrogel in promoting bone regeneration and inhibiting infection *in vivo*.

3.5. In vivo animal experiments

3.5.1. Establishment of an infected bone defect model

All rabbits exhibited satisfactory postoperative recovery without any additional complications. Prior to the operation, three rabbits from the CON group and three rabbits untreated with *S. aureus* (Untreated) were randomly selected for blood routine examinations before the operation (0 d) and at 3, 7, 10, and 14 d after operation. We also examined the wounds of rabbits in the CON group and obtained radial specimens and images. As shown in Figs. S3A and S3B, within 14 d after the operation, the white blood cell (WBC) and neutrophil (NE) counts increased over time in the CON group with *S. aureus*, indicating a state of inflammation in the body. In contrast, no significant changes in the WBC and NE counts were observed over time in the Untreated group. Imaging revealed the presence of sinus and purulent discharge at the wound site in the CON group (Fig. S3C), and an abscess formed at the defect site (Figure. S3D), confirming the successful establishment of an infected bone defect model in the radius.

3.5.2. Imaging analyses

X-ray images of the defect area in the radius were obtained at 8 and 12 weeks after surgery. As shown in Fig. 5A, no discernible bone regeneration was observed in the defect area of the CON group at 8 weeks after surgery, and the bone regeneration after 12 weeks was minor compared with the C85-Q15/H group. Moreover, no bony connection was formed at the broken ends of the fractures in CON group at 12 weeks, providing evidence of nonunion formation. In the C/H group, a bony callus was observed at 8 weeks after surgery, and a small amount of new bone was formed at 12 weeks. From 8 to 12 weeks after surgery, the new bone mass increased rapidly in the C85-Q15/H group.

To further analyze bone regeneration at the defect site, micro-CT was performed at 8 and 12 weeks after surgery (Fig. 5B). Similar to the X-ray results, almost no new bone was found in the CON group at 8 weeks, and the amount of regenerated bone remained low even at 12 weeks. In the C/H group, despite the occurrence of new bone formation between 8 and 12 weeks, healing was delayed at the fracture site. In contrast, continuous cortical bone formation was observed from weeks 8–12 in the C85-Q15/H group, indicating intact bone regeneration in the defect area. The quantitative analysis of the micro-CT images further support these results; the BV/TV value in the C85-Q15/H group was 47.48 % ± 5.62 % at 8 weeks, significantly higher than those in the C/H group (22.83 % ± 2.50 %, $p < 0.01$) and CON group (22.83 % ± 2.50 %, $p < 0.01$). Moreover, at 12 weeks, the BV/TV value in the C85-Q15/H group was 54.97 % ± 3.87 %, significantly higher than those in the C/H group 33.10 % ± 1.28 % ($p < 0.001$) and CON group 17.70 % ± 2.20 % ($p < 0.01$). Although there were significant increases in the C/H group compared with the CON group at 12 weeks ($p < 0.01$), the BV/TV value in C/H group was still less than the C85-Q15/H group ($p < 0.01$). The trends in Tb. Sp values were similar to those in BV/TV; the Tb. Sp value

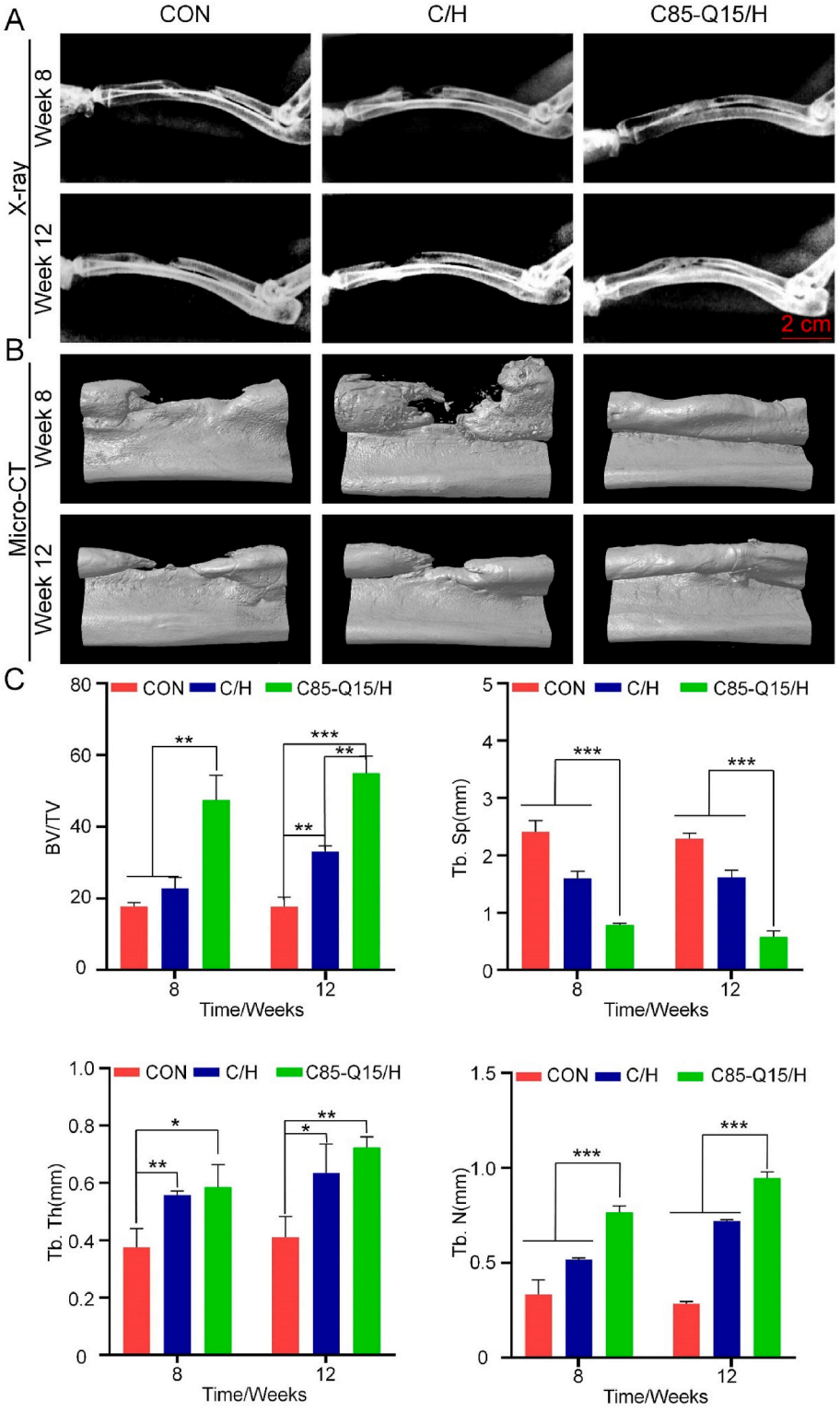

Fig. 5. Imaging results at 8 and 12 weeks after surgery. A. Representative X-ray images from the CON, C/H, and C85-Q15/H groups at 8 and 12 weeks. B. Reconstructed micro-CT images at 8 and 12 weeks. C. Analysis results of BV/TV, Tb. Sp, Tb. Th, and Tb. N. (*, $p < 0.05$; **, $p < 0.01$; ***, $p < 0.001$) (Data are expressed as mean ± SD ($n = 3$)).

in the C85-Q15/H group was significantly lower than those in the C/H and CON groups at 8 and 12 weeks ($p < 0.001$). In addition, the Tb. N value in the C85-Q15/H group was significantly higher than those of the C/H and CON groups ($p < 0.001$). The Tb. Th values of the C85-Q15/H group were higher than those of the C/H and CON groups at both 8 and 12 weeks (Fig. 5C). The unsatisfactory outcomes observed in the C/H and CON groups may be attributed to infection resulting from the absence of antibacterial activity *in vivo*. The inflammation caused by infection can impair the process of bone regeneration and increase bone resorption [10]. The *in vivo* results confirm that the composite hydrogel can promote bone regeneration in an animal model and promote the formation of callus.

Following imaging examination, the hydrogel specimens were decalcified for histological and immunohistochemical staining to further assess their *in vivo* antibacterial and osteogenic properties.

3.5.3. Histological and immunohistochemical analyses

We collected granulation tissues from the defect sites and conducted plate cultures and Giemsa staining to evaluate antibacterial efficacy *in vivo*. In the C85-Q15/H group, bacterial colonies were scarce at 8 weeks after surgery, as illustrated in Fig. 6A. In contrast, in the CON and C/H groups, prominent *S. aureus* colonies were observed. From 8 to 12 weeks, the colony density increased significantly in the CON and C/H groups but remained unchanged in the C85-Q15/H group. Giemsa staining was used to further evaluate the associated infection. At 8 and 12 weeks after surgery, *S. aureus* was absent in the C85-Q15/H group, whereas the amount of bacteria increased with time in the CON and C/H groups. In addition, obvious inflammatory cells were found in the CON and C/H groups (Fig. 6B). In the infected state, excessive bacterial internalization results in reduced new bone formation and increased apoptosis of osteoblasts. Moreover, bacteria can adhere to biomaterials to form biofilm, rendering antibiotic treatment ineffective and complicating infection eradication [34,55]. In this context, the antibacterial properties of biomaterials were crucial for infected bone defects. QCS can inhibit the formation of biofilm by reducing the expression of *icaAD* gene of *Staphylococcus* strains, which encodes the key enzyme of biofilm synthesis [4]. Tan et al. discovered that QCS with a degree of substitution of 26 % can upregulate the expression of the *icaR* gene, which encodes a negative regulator of biofilm development. Furthermore, QCS with this degree of substitution exhibited favorable biocompatibility [56]. QCS can also effectively inhibit the activity of antibiotic-resistant bacteria, incorporating QCS into PMMA bone cement demonstrated effective treatment of methicillin-resistant Staphylococcus epidermidis-induced bone infection [57]. Therefore, our results showed that QCS with high degree of substitution can effectively inhibit infection *in vivo*. However, the specific antibacterial mechanism of QCS still needs to be clarified more deeply, which will be carried out in our subsequent research.

After confirming the antibacterial properties of the hydrogel through *in vivo* experiments, we further performed H&E and Masson staining to evaluate the osteogenic properties *in vivo*. As shown in Fig. 7A, H&E staining was conducted to illustrate the morphology and microstructure of bone. At 8 weeks after surgery, minimal evidence of fresh bone regeneration was observed in the CON group, and the defect area was full of fibrous tissue. In the C/H group, partial bone regeneration occurred at the margin, whereas the defect site remained spacious. In contrast, bone regeneration was evident in the C85-Q15/H group, and the trabecular bone exhibited a well-preserved morphology. At 12 weeks after surgery, little bone regeneration was observed in the CON group, and a large amount of fibrous tissue remained. Limited osteogenesis was observed at the defect site in the C/H group after 12 weeks. In contrast, the trabeculae in the C85-Q15/H group showed higher density, regularity, and integrity. The Masson staining results reflect the maturity of collagen in the bone tissues. The color of stained bone tissue changes from blue to red as the bone matures; new bone tissue appears blue, whereas mature bone tissue appears red [58]. At 8 weeks after surgery,

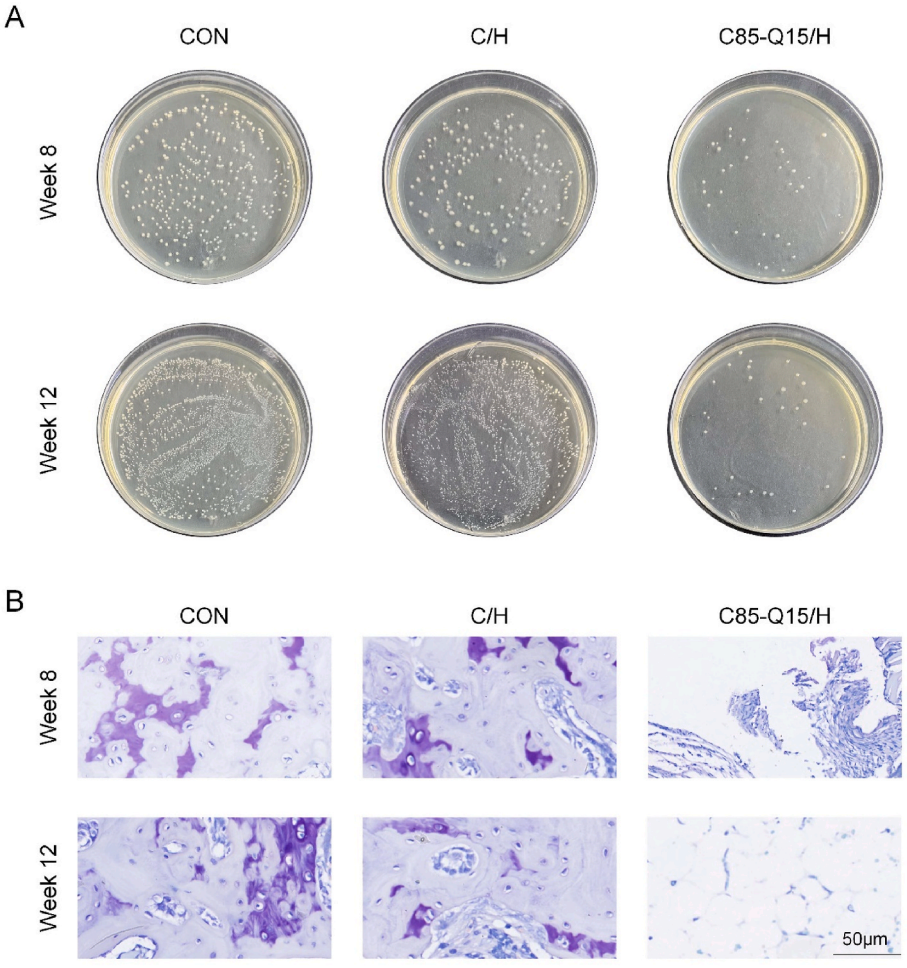

Fig. 6. Examination of *in vivo* antibacterial properties. A. *S. aureus* colonies in the granulation tissue at the defect site. B. Giemsa staining images obtained at 8 and 12 weeks after surgery.

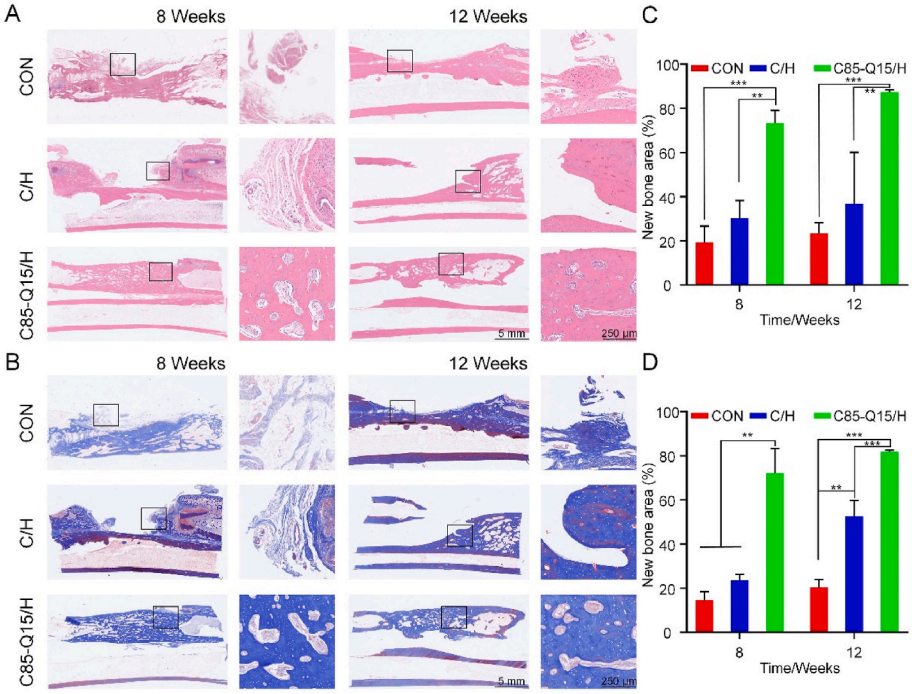

Fig. 7. Histological staining images, including the general view (left) and partial enlarged view (right), obtained at 8 and 12 weeks after surgery. A. H&E staining images of bone tissue at 8 and 12 weeks. B. Masson staining images of decalcified bone at 8 and 12 weeks after surgery. C. Quantitative analysis of new bone area in the H&E staining images at 8 and 12 weeks. D. Quantitative analysis of new bone area in the Masson staining images at 8 and 12 weeks (*, $p < 0.05$; **, $p < 0.01$; ***, $p < 0.001$) (Data are expressed as mean ± SD ($n = 3$)).

more new bone tissue was observed in the C85-Q15/H group than in the C/H group. And at 12 weeks, the regenerated bone tissues in the C85-Q15/H group had increased which had well new bone regeneration. Although new bone formation was also observed in the C/H group at 12 weeks, the amount of new bone was lower than in the C85-Q15/H group (Fig. 7B). To quantitatively evaluate bone regeneration *in vivo*, the area of new bone in the stained section was calculated using Image J software. At 8 and 12 weeks after surgery, the new bone area in the C85-Q15/H group was significantly higher than those in the C/H and CON groups based on the H&E staining images (Fig. 7C). Based on the Masson staining images, the C85-Q15/H group showed more new bone formation than the CON and C/H groups at 8 weeks ($p < 0.001$).The amount of new bone formation was higher in the C/H group than in the CON group at 12 weeks ($p < 0.01$); however, the new bone mass in the C/H group still had a significant difference compared with C85-Q15/H ($p < 0.001$; Fig. 7D). These results demonstrate that the C85-Q15/H hydrogel has a strong ability to promote trabecular bone formation and can also augment collagen production compared with the C/H hydrogel.

Bone formation was further confirmed by immunohistochemical analysis using RUNX2 and OCN as indicators. At 8 weeks after surgery, the expression of RUNX2 was significantly higher in the C85-Q15/H group than in the other two groups. At 12 weeks after surgery, the positively stained cells were increased in the C85-Q15/H group compared with the CON and C/H groups, demonstrating the good bone quality (Fig. 8A). Moreover, more positively stained cells for OCN expression were observed at 8 and 12 weeks in the C85-Q15/H group compared with the CON and C/H groups. Mature bone tissues were clearly evident, demonstrating significant osteogenic activity (Fig. 8B). Furthermore, the positive staining areas were calculated for both RUNX2 and OCN. The RUNX2-positive area in the C85-Q15/H group at 8 weeks was 52.15 % ± 2.83 %, significantly higher than those in the CON and C/H groups (10.33 % ± 0.79 % and 14.07 % ± 1.32 %, respectively; $p < 0.001$). At 12 weeks, these differences between the C85-Q15/H group and the CON and C/H groups were further increased ($p < 0.001$; Fig. 8C). Consistently, as shown in Fig. 8D, the positive areas of OCN protein expression in the C85-Q15/H group at 8 and 12 weeks were 21.05 % ± 5.17 % and 31.02 % ± 7.60 %, respectively, greater than those in the CON group (11.72 % ± 2.58 % and 9.10 % ± 5.59 %, respectively; $p < 0.05$). The expressions of OCN in the C/H group at 8 and 12 weeks (7.00 % ± 0.39 % and 20.79 % ± 3.57 %, respectively) were also lower than those in the C85-Q15/H group ($p < 0.05$). These results confirm that the C85-Q15/H hydrogel can promote bone regeneration by up-regulating the expressions of RUNX2 and OCN. In summary, the *in vivo* experimental results confirm that the C85-Q15/H group had the best antibacterial and osteogenic properties among the groups.

The bone repair ability of an orthopedic scaffold is important for the reconstruction of damaged bone tissue, and the scaffold must also have low cytotoxicity and satisfactory biocompatibility [59]. After injection into the defect area, the C85-Q15/H hydrogel showed good biocompatibility and effectively promoted bone regeneration. This may be attributed to the mixture of QCS and CS, which provides abundant positive charges to facilitate cell adhesion. Moreover, CS has been shown to improve bone healing through the expression of some osteogenesis-related genes mediated by RUNX2 [60]. Our *in vivo* results confirmed that QCS can up-regulate the expression of RUNX2 more than CS in an infected environment. The increase in RUNX2 expression can induce the expression of the anti-apoptosis Bcl-2 gene and protect osteoblasts from apoptosis damage in inflammatory reaction, thereby promoting bone regeneration [61]. In addition, nHA is a component of natural bone and has a large surface area. The introduction of nHA promotes the expression of cell adhesion proteins and effectively facilitates osteoblast adhesion and proliferation, leading to increased osteogenic ability [62,63]. Another essential factor in the bone regeneration ability of the hydrogel is its excellent antibacterial activity. The antibacterial property of the C85-Q15/H hydrogel against *S. aureus* was sustained *in vivo* for 12 weeks. Moreover, we obtained a balance between anti-infection activity and cytotoxicity by adjusting the proportion of CS and QCS, thereby optimizing the osteogenic performance. The nHA does

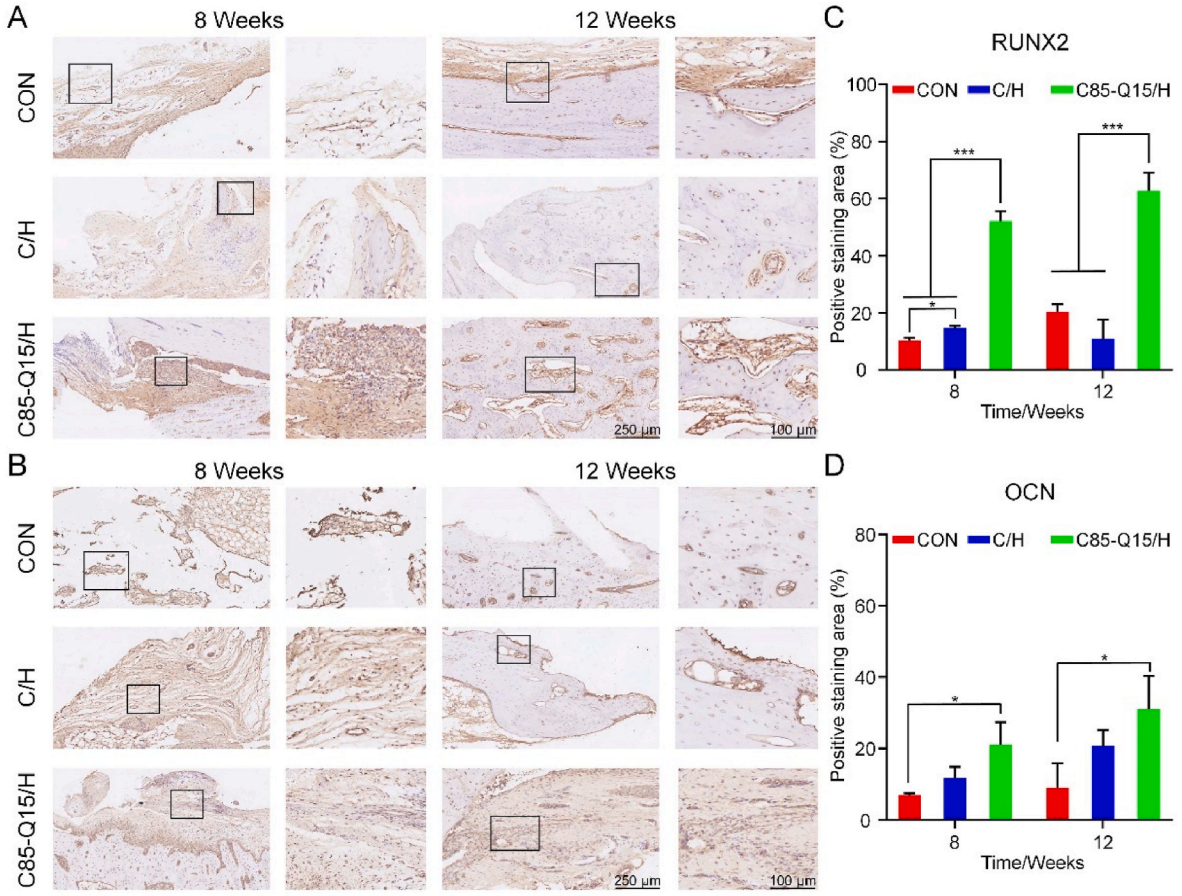

Fig. 8. Immunohistochemistry staining images of RUNX2 and OCN. A. Representative immunohistochemistry staining images of RUNX2 at 8 and 12 weeks after surgery. B. Representative immunohistochemistry staining images of OCN at 8 and 12 weeks after surgery. C. Semi-quantitative analysis of the RUNX2-positive staining area. D. Semi-quantitative analysis of the OCN-positive staining area (*, $p < 0.05$; ***, $p < 0.001$) (Data are expressed as mean ± SD ($n = 3$)).

not have any antibacterial property. Therefore, on one hand, the osteogenic performance of the hydrogel is attributed to the strong antibacterial activity of QCS, which eliminates local bacteria in the early stage and promotes osteoblast adhesion. On the other hand, the CS and QCS cooperate with nHA to further promote osteoblast differentiation and bone regeneration.

This study is subject to certain limitations because it only investigated the effect of one single type of degree of substitution of QCS on the antibacterial and osteogenic properties of the hydrogel. Alterations in the degree of substitution of QCS can significantly affect the water solubility, antibacterial efficacy, and cytotoxicity [64]. Therefore, future research should prioritize achieving an optimal balance between the biocompatibility and antibacterial properties of QCS with varying degrees of substitution when combined with CS in different proportions to identify the most effective therapeutic approach for treating infected bone defects.

4. Conclusions

In this study, we synthesized thermosensitive CS-QCS hydrogels incorporating nHA based on CS/β-GP hydrogels. Compared to the pure CS hydrogel, the C85-Q15/H hydrogel containing 85 % CS and 15 % QCS exhibited a strong antibacterial property along with favorable biocompatibility. Loading with nHA further enhanced the osteogenic property of the hydrogel and upregulated the expressions of osteogenic genes *in vitro*. *In vivo* experiments in an infected bone defect model demonstrated that C85-Q15/H has dual antibacterial and osteogenic functions. In summary, this dual-functional hydrogel can promote bone regeneration and degrade in an infected environment, greatly reducing the risk of reinfection caused by additional operation. This study has significant clinical transformation potential and provides a promising treatment strategy for bone defect infection.

Funding

This work was supported by the 13th Five-Year Plan of Science and Technology Research of Jilin Provincial Education Department (JJKH20180108KJ), the project of Jilin Provincial Science and Technology Department (20230402009 GH) and Industrial Technology Research and Development Project of Jilin Provincial Development and Reform Commission (2023C040-3).

CRediT authorship contribution statement

Yuhang Tian: Conceptualization, Investigation, Writing – original draft. **Yutao Cui:** Writing – review & editing. **Guangkai Ren:** Data curation. **Yi Fan:** Methodology, Validation. **Minghan Dou:** Validation. **Shaorong Li:** Validation. **Gan Wang:** Supervision. **Yanbing Wang:** Conceptualization. **Chuangang Peng:** Methodology, Validation. **Dankai Wu:** Conceptualization, Funding acquisition, Supervision, Writing – review & editing.

Declaration of competing interest

The authors declare that they have no known competing financial interests or personal relationships that could have appeared to influence

the work reported in this paper.

Data availability

Data will be made available on request.

Appendix A. Supplementary data

Supplementary data to this article can be found online at https://doi.org/10.1016/j.mtbio.2024.100972.

References

[1] P. Wei, W. Jing, Z. Yuan, Y. Huang, B. Guan, W. Zhang, X. Zhang, J. Mao, Q. Cai, D. Chen, X. Yang, Vancomycin- and Strontium-loaded microspheres with Multifunctional activities against bacteria, in angiogenesis, and in osteogenesis for enhancing infected bone regeneration, ACS Appl. Mater. Interfaces 11 (2019) 30596–30609, https://doi.org/10.1021/acsami.9b10219.

[2] W.T. Jia, Q. Fu, W.H. Huang, C.Q. Zhang, M.N. Rahaman, Comparison of borate bioactive glass and calcium Sulfate as implants for the local delivery of teicoplanin in the treatment of methicillin-resistant Staphylococcus aureus-induced osteomyelitis in a rabbit model, Antimicrob. Agents Chemother. 59 (2015) 7571–7580, https://doi.org/10.1128/AAC.00196-15.

[3] J. Ristiniemi, M. Lakovaara, T. Flinkkila, P. Jalovaara, Staged method using antibiotic beads and subsequent autografting for large traumatic tibial bone loss: 22 of 23 fractures healed after 5-20 months, Acta Orthop. 78 (2007) 520–527, https://doi.org/10.1080/17453670710014176.

[4] Z.X. Peng, B. Tu, Y. Shen, L. Du, L. Wang, S.R. Guo, T.T. Tang, Quaternized chitosan inhibits icaA transcription and biofilm formation by Staphylococcus on a titanium surface, Antimicrob. Agents Chemother. 55 (2011) 860–866, https://doi.org/10.1128/AAC.01005-10.

[5] K.-T. Peng, C.-F. Chen, I.M. Chu, Y.-M. Li, W.-H. Hsu, R.W.-W. Hsu, P.-J. Chang, Treatment of osteomyelitis with teicoplanin-encapsulated biodegradable thermosensitive hydrogel nanoparticles, Biomaterials 31 (2010) 5227–5236, https://doi.org/10.1016/j.biomaterials.2010.03.027.

[6] J.S. McLaren, L.J. White, H.C. Cox, W. Ashraf, C.V. Rahman, G.W. Blunn, A. E. Goodship, R.A. Quirk, K.M. Shakesheff, R. Bayston, B.E. Scammell, A biodegradable antibiotic-impregnated scaffold to prevent osteomyelitis in a contaminated in vivo bone defect model, Eur. Cell. Mater. 27 (2014) 332–349, https://doi.org/10.22203/ecm.v027a24.

[7] R. LogithKumar, A. KeshavNarayan, S. Dhivya, A. Chawla, S. Saravanan, N. Selvamurugan, A review of chitosan and its derivatives in bone tissue engineering, Carbohydr. Polym. 151 (2016) 172–188, https://doi.org/10.1016/j.carbpol.2016.05.049.

[8] L. Keller, A. Regiel-Futyra, M. Gimeno, S. Eap, G. Mendoza, V. Andreu, Q. Wagner, A. Kyziol, V. Sebastian, G. Stochel, M. Arruebo, N. Benkirane-Jessel, Chitosan-based nanocomposites for the repair of bone defects, Nanomedicine 13 (2017) 2231–2240, https://doi.org/10.1016/j.nano.2017.06.007.

[9] J.K. McEwan, H.C. Tribe, N. Jacobs, N. Hancock, A.A. Qureshi, D.G. Dunlop, R. O. Oreffo, Regenerative medicine in lower limb reconstruction, Regen. Med. 13 (2018) 477–490, https://doi.org/10.2217/rme-2018-0011.

[10] Y. Cui, H. Liu, Y. Tian, Y. Fan, S. Li, G. Wang, Y. Wang, C. Peng, D. Wu, Dual-functional composite scaffolds for inhibiting infection and promoting bone regeneration, Mater Today Bio 16 (2022) 100409, https://doi.org/10.1016/j.mtbio.2022.100409.

[11] J.A. Inzana, E.M. Schwarz, S.L. Kates, H.A. Awad, Biomaterials approaches to treating implant-associated osteomyelitis, Biomaterials 81 (2016) 58–71, https://doi.org/10.1016/j.biomaterials.2015.12.012.

[12] W.-T. Jia, X. Zhang, S.-H. Luo, X. Liu, W.-H. Huang, M.N. Rahaman, D.E. Day, C.-Q. Zhang, Z.-P. Xie, J.-Q. Wang, Novel borate glass/chitosan composite as a delivery vehicle for teicoplanin in the treatment of chronic osteomyelitis, Acta Biomater. 6 (2010) 812–819, https://doi.org/10.1016/j.actbio.2009.09.011.

[13] M. Prabaharan, Chitosan derivatives as promising materials for controlled drug delivery, J. Biomater. Appl. 23 (2008) 5–36, https://doi.org/10.1177/0885328208091562.

[14] H.Y. Zhou, L.J. Jiang, P.P. Cao, J.B. Li, X.G. Chen, Glycerophosphate-based chitosan thermosensitive hydrogels and their biomedical applications, Carbohydr. Polym. 117 (2015) 524–536, https://doi.org/10.1016/j.carbpol.2014.09.094.

[15] J. Cho, M.C. Heuzey, A. Begin, P.J. Carreau, Physical gelation of chitosan in the presence of beta-glycerophosphate: the effect of temperature, Biomacromolecules 6 (2005) 3267–3275, https://doi.org/10.1021/bm050313s.

[16] S. Saravanan, S. Vimalraj, P. Thanikaivelan, S. Banudevi, G. Manivasagam, A review on injectable chitosan/beta glycerophosphate hydrogels for bone tissue regeneration, Int. J. Biol. Macromol. 121 (2019) 38–54, https://doi.org/10.1016/j.ijbiomac.2018.10.014.

[17] F. Croisier, C. Jérôme, Chitosan-based biomaterials for tissue engineering, Eur. Polym. J. 49 (2013) 780–792, https://doi.org/10.1016/j.eurpolymj.2012.12.009.

[18] M.S. Riaz Rajoka, L. Zhao, H.M. Mehwish, Y. Wu, S. Mahmood, Chitosan and its derivatives: synthesis, biotechnological applications, and future challenges, Appl. Microbiol. Biotechnol. 103 (2019) 1557–1571, https://doi.org/10.1007/s00253-018-9550-z.

[19] T. Chen, R. Wang, L.Q. Xu, K.G. Neoh, E.T. Kang, Carboxymethyl chitosan-functionalized magnetic nanoparticles for Disruption of biofilms of Staphylococcus aureus and Escherichia coli, Ind. Eng. Chem. Res. 51 (2012) 13164–13172, https://doi.org/10.1021/ie301522w.

[20] S.L. Levengood, M. Zhang, Chitosan-based scaffolds for bone tissue engineering, J. Mater. Chem. B 2 (2014) 3161–3184, https://doi.org/10.1039/C4TB00027G.

[21] W. Sajomsang, S. Tantayanon, V. Tangpasuthadol, W.H. Daly, Quaternization of N-aryl chitosan derivatives: synthesis, characterization, and antibacterial activity, Carbohydr. Res. 344 (2009) 2502–2511, https://doi.org/10.1016/j.carres.2009.09.004.

[22] B. Shagdarova, A. Lunkov, A. Il'ina, V. Varlamov, Investigation of the properties of N-[(2-hydroxy-3-trimethylammonium) propyl] chloride chitosan derivatives, Int. J. Biol. Macromol. 124 (2019) 994–1001, https://doi.org/10.1016/j.ijbiomac.2018.11.209.

[23] Z.-X. Peng, L. Wang, L. Du, S.-R. Guo, X.-Q. Wang, T.-T. Tang, Adjustment of the antibacterial activity and biocompatibility of hydroxypropyltrimethyl ammonium chloride chitosan by varying the degree of substitution of quaternary ammonium, Carbohydrate Polymers 81 (2010) 275–283, https://doi.org/10.1016/j.carbpol.2010.02.008.

[24] Y. Tian, D. Wu, D. Wu, Y. Cui, G. Ren, Y. Wang, J. Wang, C. Peng, Chitosan-based biomaterial scaffolds for the repair of infected bone defects, Front. Bioeng. Biotechnol. 10 (2022) 899760, https://doi.org/10.3389/fbioe.2022.899760.

[25] D.B. Lima, M.A.A. de Souza, G.G. de Lima, E.P. Ferreira Souto, H.M.L. Oliveira, M. V.L. Fook, M.J.C. de Sa, Injectable bone substitute based on chitosan with polyethylene glycol polymeric solution and biphasic calcium phosphate microspheres, Carbohydr. Polym. 245 (2020) 116575, https://doi.org/10.1016/j.carbpol.2020.116575.

[26] M. Shakir, R. Jolly, A.A. Khan, S.S. Ahmed, S. Alam, M.A. Rauf, M. Owais, M. A. Farooqi, Resol based chitosan/nano-hydroxyapatite nanoensemble for effective bone tissue engineering, Carbohydr. Polym. 179 (2018) 317–327, https://doi.org/10.1016/j.carbpol.2017.09.103.

[27] Y. Yang, S. Yang, Y. Wang, Z. Yu, H. Ao, H. Zhang, L. Qin, O. Guillaume, D. Eglin, R.G. Richards, T. Tang, Anti-infective efficacy, cytocompatibility and biocompatibility of a 3D-printed osteoconductive composite scaffold functionalized with quaternized chitosan, Acta Biomater. 46 (2016) 112–128, https://doi.org/10.1016/j.actbio.2016.09.035.

[28] Q.X. Ji, X.G. Chen, Q.S. Zhao, C.S. Liu, X.J. Cheng, L.C. Wang, Injectable thermosensitive hydrogel based on chitosan and quaternized chitosan and the biomedical properties, J. Mater. Sci. Mater. Med. 20 (2009) 1603–1610, https://doi.org/10.1007/s10856-009-3729-x.

[29] A. Wubneh, E.K. Tsekoura, C. Ayranci, H. Uludag, Current state of fabrication technologies and materials for bone tissue engineering, Acta Biomater. 80 (2018) 1–30, https://doi.org/10.1016/j.actbio.2018.09.031.

[30] R. Li, Y. Sun, Z. Cai, Y. Li, J. Sun, W. Bi, F. Yang, Q. Zhou, T. Ye, Y. Yu, Highly bioactive peptide-HA photo-crosslinking hydrogel for sustained promoting bone regeneration, Chem. Eng. J. 415 (2021), https://doi.org/10.1016/j.cej.2021.129015.

[31] V. Karageorgiou, D. Kaplan, Porosity of 3D biomaterial scaffolds and osteogenesis, Biomaterials 26 (2005) 5474–5491, https://doi.org/10.1016/j.biomaterials.2005.02.002.

[32] J. Wu, Z.G. Su, G.H. Ma, A thermo- and pH-sensitive hydrogel composed of quaternized chitosan/glycerophosphate, Int. J. Pharm. 315 (2006) 1–11, https://doi.org/10.1016/j.ijpharm.2006.01.045.

[33] F. Wahid, H.S. Wang, C. Zhong, L.Q. Chu, Facile fabrication of moldable antibacterial carboxymethyl chitosan supramolecular hydrogels cross-linked by metal ions complexation, Carbohydr. Polym. 165 (2017) 455–461, https://doi.org/10.1016/j.carbpol.2017.02.085.

[34] Q. Ou, K. Huang, C. Fu, C. Huang, Y. Fang, Z. Gu, J. Wu, Y. Wang, Nanosilver-incorporated halloysite nanotubes/gelatin methacrylate hybrid hydrogel with osteoimmunomodulatory and antibacterial activity for bone regeneration, Chem. Eng. J. 382 (2020), https://doi.org/10.1016/j.cej.2019.123019.

[35] W.W. Thein-Han, R.D.K. Misra, Biomimetic chitosan–nanohydroxyapatite composite scaffolds for bone tissue engineering, Acta Biomater. 5 (2009) 1182–1197, https://doi.org/10.1016/j.actbio.2008.11.025.

[36] Y.-W. Ge, M. Chu, Z.-Y. Zhu, Q.-F. Ke, Y.-P. Guo, C.-Q. Zhang, W.-T. Jia, Nacre-inspired magnetically oriented micro-cellulose fibres/nano-hydroxyapatite/chitosan layered scaffold enhances pro-osteogenesis and angiogenesis, Materials Today Bio 16 (2022), https://doi.org/10.1016/j.mtbio.2022.100439.

[37] A. Sadeghianmaryan, S. Naghieh, Z. Yazdanpanah, H. Alizadeh Sardroud, N. K. Sharma, L.D. Wilson, X. Chen, Fabrication of chitosan/alginate/hydroxyapatite hybrid scaffolds using 3D printing and impregnating techniques for potential cartilage regeneration, Int. J. Biol. Macromol. 204 (2022) 62–75, https://doi.org/10.1016/j.ijbiomac.2022.01.201.

[38] Y.-Q. Tang, Q.-Y. Wang, Q.-F. Ke, C.-Q. Zhang, J.-J. Guan, Y.-P. Guo, Mineralization of ytterbium-doped hydroxyapatite nanorod arrays in magnetic chitosan scaffolds improves osteogenic and angiogenic abilities for bone defect healing, Chem. Eng. J. 387 (2020), https://doi.org/10.1016/j.cej.2020.124166.

[39] X. Zhao, P. Li, B. Guo, P.X. Ma, Antibacterial and conductive injectable hydrogels based on quaternized chitosan-graft-polyaniline/oxidized dextran for tissue engineering, Acta Biomater. 26 (2015) 236–248, https://doi.org/10.1016/j.actbio.2015.08.006.

[40] D. Zhu, H. Cheng, J. Li, W. Zhang, Y. Shen, S. Chen, Z. Ge, S. Chen, Enhanced water-solubility and antibacterial activity of novel chitosan derivatives modified with quaternary phosphonium salt, Mater. Sci. Eng., C 61 (2016) 79–84, https://doi.org/10.1016/j.msec.2015.12.024.

[41] R. Sedghi, A. Shaabani, N. Sayyari, Electrospun triazole-based chitosan nanofibers as a novel scaffolds for bone tissue repair and regeneration, Carbohydr. Polym. 230 (2020) 115707, https://doi.org/10.1016/j.carbpol.2019.115707.
[42] W.-K. Jung, E. Mendis, J.-Y. Je, P.-J. Park, B.W. Son, H.C. Kim, Y.K. Choi, S.-K. Kim, Angiotensin I-converting enzyme inhibitory peptide from yellowfin sole (Limanda aspera) frame protein and its antihypertensive effect in spontaneously hypertensive rats, Food Chem. 94 (2006) 26–32, https://doi.org/10.1016/j.foodchem.2004.09.048.
[43] H. Tan, R. Ma, C. Lin, Z. Liu, T. Tang, Quaternized chitosan as an antimicrobial agent: antimicrobial activity, mechanism of action and biomedical applications in orthopedics, Int. J. Mol. Sci. 14 (2013) 1854–1869, https://doi.org/10.3390/ijms14011854.
[44] C. Qin, Q. Xiao, H. Li, M. Fang, Y. Liu, X. Chen, Q. Li, Calorimetric studies of the action of chitosan-N-2-hydroxypropyl trimethyl ammonium chloride on the growth of microorganisms, Int. J. Biol. Macromol. 34 (2004) 121–126, https://doi.org/10.1016/j.ijbiomac.2004.03.009.
[45] E. Alsberg, K.W. Anderson, A. Albeiruti, R.T. Franceschi, D.J. Mooney, Cell-interactive alginate hydrogels for bone tissue engineering, J. Dent. Res. 80 (2001) 2025–2029, https://doi.org/10.1177/00220345010800111501.
[46] X. Zhang, Y. He, P. Huang, G. Jiang, M. Zhang, F. Yu, W. Zhang, G. Fu, Y. Wang, W. Li, H. Zeng, A novel mineralized high strength hydrogel for enhancing cell adhesion and promoting skull bone regeneration in situ, Compos. B Eng. 197 (2020), https://doi.org/10.1016/j.compositesb.2020.108183.
[47] C.L. He, X.B. Jin, P.X. Ma, Calcium phosphate deposition rate, structure and osteoconductivity on electrospun poly(L-lactic acid) matrix using electrodeposition or simulated body fluid incubation, Acta Biomater. 10 (2014) 419–427, https://doi.org/10.1016/j.actbio.2013.08.041.
[48] Y. Pakzad, M. Fathi, Y. Omidi, M. Mozafari, A. Zamanian, Synthesis and characterization of timolol maleate-loaded quaternized chitosan-based thermosensitive hydrogel: a transparent topical ocular delivery system for the treatment of glaucoma, Int. J. Biol. Macromol. 159 (2020) 117–128, https://doi.org/10.1016/j.ijbiomac.2020.04.274.
[49] Y. Cui, Z. Wang, Z. Li, X. Ji, B. Yuan, Y. Sun, C. Peng, Y. Leng, M. Dou, J. Wang, H. Liu, D. Wu, Functionalized anti-osteoporosis drug delivery system enhances osseointegration of an inorganic–organic bioactive interface in osteoporotic microenvironment, Mater. Des. (2021) 206, https://doi.org/10.1016/j.matdes.2021.109753.
[50] C. Heinemann, S. Heinemann, A. Bernhardt, H. Worch, T. Hanke, Novel Textile chitosan scaffolds promote spreading, proliferation, and differentiation of osteoblasts, Biomacromolecules 9 (2008) 2913–2920, https://doi.org/10.1021/bm800693d.
[51] X. Niu, L. Wang, M. Xu, M. Qin, L. Zhao, Y. Wei, Y. Hu, X. Lian, Z. Liang, S. Chen, W. Chen, D. Huang, Electrospun polyamide-6/chitosan nanofibers reinforced nano-hydroxyapatite/polyamide-6 composite bilayered membranes for guided bone regeneration, Carbohydrate Polymers (2021) 260, https://doi.org/10.1016/j.carbpol.2021.117769.
[52] M. Wang, Y. Sa, P. Li, Y. Guo, Y. Du, H. Deng, T. Jiang, Y. Wang, A versatile and injectable poly(methyl methacrylate) cement functionalized with quaternized chitosan-glycerophosphate/nanosized hydroxyapatite hydrogels, Mater. Sci. Eng., C 90 (2018) 264–272, https://doi.org/10.1016/j.msec.2018.04.075.
[53] T.M. Liu, E.H. Lee, Transcriptional regulatory cascades in Runx2-dependent bone development, Tissue Eng., Part B 19 (2013) 254–263, https://doi.org/10.1089/ten.TEB.2012.0527.
[54] T. Komori, Regulation of proliferation, differentiation and functions of osteoblasts by Runx2, Int. J. Mol. Sci. 20 (2019), https://doi.org/10.3390/ijms20071694.
[55] J. Gu, H. Li, M. Li, C. Vuong, M. Otto, Y. Wen, Q. Gao, Bacterial insertion sequence IS as a potential molecular marker to discriminate invasive strains from commensal strains of, J. Hosp. Infect. 61 (2005) 342–348, https://doi.org/10.1016/j.jhin.2005.04.017.
[56] H. Tan, Z. Peng, Q. Li, X. Xu, S. Guo, T. Tang, The use of quaternised chitosan-loaded PMMA to inhibit biofilm formation and downregulate the virulence-associated gene expression of antibiotic-resistant staphylococcus, Biomaterials 33 (2012) 365–377, https://doi.org/10.1016/j.biomaterials.2011.09.084.
[57] H.L. Tan, H.Y. Ao, R. Ma, W.T. Lin, T.T. Tang, Effect of quaternized chitosan-loaded polymethylmethacrylate bone cement on methicillin-resistant infection of the tibial Metaphysis in a rabbit model, Antimicrob. Agents Chemother. 58 (2014) 6016–6023, https://doi.org/10.1128/Aac.03489-14.
[58] K. Zhang, S. Lin, Q. Feng, C. Dong, Y. Yang, G. Li, L. Bian, Nanocomposite hydrogels stabilized by self-assembled multivalent bisphosphonate-magnesium nanoparticles mediate sustained release of magnesium ion and promote in-situ bone regeneration, Acta Biomater. 64 (2017) 389–400, https://doi.org/10.1016/j.actbio.2017.09.039.
[59] V. Borsari, M. Fini, G. Giavaresi, M. Tschon, R. Chiesa, L. Chiusoli, A. Salito, L. Rimondini, R. Giardino, Comparativein vivoevaluation of porous and dense duplex titanium and hydroxyapatite coating with high roughnesses in different implantation environments, J. Biomed. Mater. Res. 89A (2009) 550–560, https://doi.org/10.1002/jbm.a.31995.
[60] M.H. Ho, C.J. Yao, M.H. Liao, P.I. Lin, S.H. Liu, R.M. Chen, Chitosan nanofiber scaffold improves bone healing via stimulating trabecular bone production due to upregulation of the Runx2/osteocalcin/alkaline phosphatase signaling pathway, Int. J. Nanomed. 10 (2015) 5941–5954, https://doi.org/10.2147/IJN.S90669.
[61] W.-P. Ho, W.-P. Chan, M.-S. Hsieh, R.-M. Chen, Runx2-mediatedbcl-2gene expression contributes to nitric oxide protection against hydrogen peroxide-induced osteoblast apoptosis, J. Cell. Biochem. 108 (2009) 1084–1093, https://doi.org/10.1002/jcb.22338.
[62] M. Shahrezaie, A. Moshiri, B. Shekarchi, A. Oryan, N. Maffulli, J. Parvizi, Effectiveness of tissue engineered three-dimensional bioactive graft on bone healing and regeneration: an in vivo study with significant clinical value, J Tissue Eng Regen M 12 (2018) 936–960, https://doi.org/10.1002/term.2510.
[63] J. Xu, H. Aoki, S. Kasugai, M. Otsuka, Enhancement of mineralization on porous titanium surface by filling with nano-hydroxyapatite particles fabricated with a vacuum spray method, Mater. Sci. Eng. C (2020) 111, https://doi.org/10.1016/j.msec.2020.110772.
[64] R. Wongwanakul, S. Jianmongkol, P. Gonil, W. Sajomsang, R. Maniratanachote, S. Aueviriyavit, Biocompatibility study of quaternized chitosan on the proliferation and differentiation of Caco-2 cells as an in vitro model of the intestinal barrier, J. Bioact. Compat Polym. 32 (2017) 92–107, https://doi.org/10.1177/0883911516658780.